

## Supplemental information

### **Mimicking Ion and Water Management in Poultry Breeding for Highly Reversible Zinc Ion Batteries**

*Shengli Zhai, Wanrong Song, Keren Jiang, Xuehai Tan, Wenyao Zhang, Yang Yang, Weifeng Chen, Ning Chen, Hongbo Zeng, Hui Li, and Zhi Li\**

## Experimental Procedures

**Preparation of ESM and DESM:** The fresh eggshell waste was collected from a local restaurant. The eggshell was rinsed multiple times with DI water to remove residual egg white and yolk. Subsequently, ESM was gently peeled off from the eggshell and thoroughly cleaned with DI water. The obtained ESM was boiled in DI water for 15 minutes to obtain DESM. [The ESM and DESM utilized in assembly of cells were from the body regions of the eggs to ensure a predominantly flat placement on the surface of the electrodes.](#)

**Synthesis of NVO:** NVO nanowires were synthesized via a hydrothermal method. In brief, 4 mol  $V_2O_5$  was dissolved in 85 mL NaOH solution containing 4 mmol NaOH. The resulting mixture was magnetically stirred for 1h, followed by being transferred into a Teflon-lined autoclave bomb. Subsequently, the autoclave bomb was placed into an electric oven at 180 °C for 6h. After cooling down to room temperature, the prepared products were washed with distilled water and ethanol several times and dried at 60 °C to obtain NVO.

**Electrochemical measurements:** Commercial Zn, Cu foils, ESM, and DESM were punched into circular disks with a diameter of ~1.3 cm. Then, the obtained Zn and Cu disks were alternately polished with sandpapers and rinsed with water to remove passivation layers and smooth the surface concurrently. The polished Zn and Cu disks were denoted as bare Zn and Cu electrodes, respectively. Symmetric Zn/Zn, Zn/Cu, and Zn/NVO full cells are based on CR-2032 type coin cells, and all batteries were assembled in the open air and aged for 6h before electrochemical measurement. Glass fiber (GE-Whatman) paper was used as the separator, and 120  $\mu$ L 2M  $ZnSO_4$  worked as an electrolyte. In some cells, ESM or DESM serves as a protection layer for electrodes. For Zn/NVO full batteries, the cathode materials were prepared by mixing NVO with 20 wt.% carbon black and 10 wt.% polyvinylidene fluoride (PVDF) in N-methyl pyrrolidone (NMP) to form a homogeneous slurry. The well-mixed slurry was coated on the carbon paper and vacuum dried at 90 °C overnight. The GCD profiles were recorded on a multichannel-current static system (Arbin Instruments BT 2000, College Station, TX, USA). The CV curves, electrochemical impedance spectroscopy (EIS), and linear sweep voltammetry (LSV) curves were collected on a Solartron 1470E Multichannel Potentiostat/Cell Test System. EIS was performed in a frequency range of 100 kHz to 10 mHz with a voltage amplitude of 10 mV. The electrochemical corrosion of the Zn anode is analyzed via Tafel plots by performing LSV in a three-electrode system consisting of Zn foil as the working electrode, graphite rod as the counter electrode, saturated calomel electrode (SCE) as reference electrode, and 2M  $ZnSO_4$  as electrolyte. The HER behaviors were evaluated by the same set-up except using 2M  $Na_2SO_4$  as an electrolyte. The ionic conductivity of ESM and DESM was determined by EIS spectra.

The EIS was performed by using a two-electrode set-up consisting of two identical Ti foil and 2M ZnSO<sub>4</sub> electrolytes which were assembled in a CR-2032 type coin cell. The real impedance at the highest frequency was taken as the bulk resistance. The equation of ionic conductivity can be expressed as  $\sigma = L/RA$ , where  $\sigma$  is conductivity, and L, R, and A represent the thickness of protein film, the bulk resistance of, and the area of stainless steel sheet electrode, respectively.

**Materials characterization:** The microstructure and elemental mapping of the samples were investigated by a Field Emission Scanning Electron Microscope (FESEM, Zeiss Sigma FESEM w/EDX&EBSD). The chemical compositions are characterized by FESEM and Kratos AXIS ULTRADLD (XPS, Al K $\alpha$  radiation) spectrometer, and an Inductively Coupled Plasma-Optical Emission Spectroscopy (ICP-OES, Thermo iCAP6300 Duo). All the XPS spectra were calibrated to the adventitious hydrocarbon (AdvHC) carbon peak at 284.8 eV. The XRD patterns were recorded by using a Rigaku XRD Ultima IV diffractometer (Cu K $\alpha$  radiation). The FTIR spectra were obtained by employing Nicolet 6700 spectrometer under ATR mode. The In-situ fluorescence images of ESM and DESM were taken by a Zeiss Axiovert 100M fluorescent microscope. The heating device was constructed using an aluminum rectangular tube containing embedded heating elements. Electric drills were employed to create multiple slots on the outer surface of the aluminum rectangular tube. The wet ESM was then carefully transferred into a slot filled with DI water. The heating element was powered by a portable power supply with a maximum temperature capacity of 220 °C. Following this, a cover slip was positioned atop the slot to facilitate the capture of fluorescent images. Atomic force microscopy (AFM) topography characterization was performed using the Peak Force Quantitative Nanomechanical (PF-QNM) mode with Dimension Icon instrument (Bruker Corporation, Santa Barbara, CA, USA) equipped with a VTESPA-70 probe ( $k=2.3 \text{ N m}^{-1}$ ).

**XAFS measurement and analysis:** Both ESM and DESM were immersed in a 2M ZnSO<sub>4</sub> electrolyte for an extended duration to ensure the thorough absorption of Zn<sup>2+</sup>. Subsequently, the samples underwent a gentle rinse with DI water before being securely sealed within the sample holder slots using Kapton tape for XAFS characterization. The reference powder samples were sealed in the XAFS sample holder slots using the same method. Zn and V K-edge XAFS spectra were collected on the 06ID superconducting wiggler sourced hard X-ray microanalysis (HXMA) beamline at the Canadian Light Source with a configuration of an Rh-coated collimating mirror, a Si double crystal (111) monochromator, and an Rh coated toroidal mirror in sequence. All the experiment was performed under fluorescence mode. The photon energy was in-step calibrated by using Zn or V metallic reference sample from Exafs Materials

(<http://exafsmaterials.com/Contact.html>). The collected XAFS raw data were normalized, background-subtracted, and Fourier-transformed based on the standard procedures using the ATHENA program.<sup>1, 2</sup> Least-squares curve fitting analysis of the EXAFS data was performed using the ARTEMIS program according to standard procedures to get the quantitative structural parameters.<sup>2</sup> The k3-weighted EXAFS spectra were obtained by normalizing to the edge-jump step and subtracting the post-edge background from the overall absorption. Then,  $\chi(k)$  data of Zn or V K-edge in the k-space was Fourier transformed to real (R) space using a Hanning window ( $dk=1.0 \text{ \AA}^{-1}$ ) to separate the EXAFS contributions from different coordination shells.

**DFT calculation:** All the DFT calculations were performed using the Gaussian 09 program.<sup>3</sup> The geometry optimizations were carried out at the B3LYP/6-311++G(d,p)<sup>4</sup> level of the theory. The vibrational frequency was calculated to confirm that the optimized geometries were local minima without any imaginary frequencies. The single point energies of the optimized structures were calculated at the M06-2X/6-311++G(d,p)<sup>5</sup> level. The polarizable continuum model (PCM)<sup>6</sup> model was used in the optimizations of all the complexes to simulate the water environment. The binding energy ( $E_b$ ) of ALA and  $Zn^{2+}$  was calculated using the following equation:

$$E_b = E_{[Zn(ALA-ALA)(H_2O)_x]^{2+}} - (E_{ALA-ALA} + E_{[Zn(H_2O)_x]^{2+}})$$

where  $E_{[Zn(ALA-ALA)(H_2O)_x]^{2+}}$ ,  $E_{ALA-ALA}$ ,  $E_{[Zn(H_2O)_x]^{2+}}$  are the energies of  $[Zn(ALA-ALA)(H_2O)_x]^{2+}$ , ALA-ALA,  $[Zn(H_2O)_x]^{2+}$ , complexes, respectively.

The binding energy ( $E_b$ ) of  $H_2O$  and  $Zn^{2+}$  in  $[Zn(H_2O)_5]^{2+}$  complexes was calculated using the following equation:

$$E_b = E_{[Zn(H_2O)_6]^{2+}} - (E_{[Zn(H_2O)_5]^{2+}} + E_{H_2O})$$

where  $E_{[Zn(H_2O)_6]^{2+}}$ ,  $E_{[Zn(H_2O)_5]^{2+}}$  and  $E_{H_2O}$  are the energies of the  $[Zn(H_2O)_6]^{2+}$ ,  $[Zn(H_2O)_5]^{2+}$  complexes, and  $H_2O$ , respectively.

**SR- $\mu$ CT:** Tomography image was performed at the Biomedical Imaging and Therapy-Bending Magnet beamline (BMIT-BM 05B1-1) at the Canadian Light Source. The 05B1-1 bending magnet generates X-rays in the energy range of 12.6-40 keV. It gives a maximum pixel size of 0.72  $\mu$ m. The SR- $\mu$ CT images of ESM, DESM, glass fiber separators, and Zn electrodes were obtained by using an in-situ cell as schematically shown in Fig. S21. The in-situ cells were constructed using polyimide rods, and a tap was used to thread a hole (3.85 mm) in the

polyamide rod. The stainless steel threaded rod with one end polished was used as current collectors. Polished Zn sheets, ESM, and DESM were punched into circular disks with a diameter of  $\sim 2.00$  mm, and the glassy fiber paper was punched into circulars with a slightly larger diameter. For the symmetric cells, all the components were assembled into a homemade cell with a sandwiched structure same as that in coins cells. The order of layers for the in-situ cells is outlined in Fig. S21. The cell was mounted on a Huber manual goniometer head with double-sided tape. Sets of projection images (sample in beam path) were collected through  $180^\circ$  rotation of the sample. Image processing and three-dimensional reconstructions for this paper were generated using Dragonfly software, Version 2021.3 for [Windows]. Object Research Systems (ORS) Inc, Montreal, Canada, 2021; software available at <http://www.theobjects.com/dragonfly>.

**Preparation of DESM/glassy fiber/cellulose nanofiber membranes:** DESM and DI water were filled into a blender container followed by blending for 10 min. Next, 20 wt% glass fiber and 10 wt% cellulose nanofibers were added to the DESM dispersion and sonicated for 10 minutes. The resulting mixture was filtered to obtain the DESM/glassy fiber/cellulose nanofiber membranes, which were then vacuum-dried overnight.

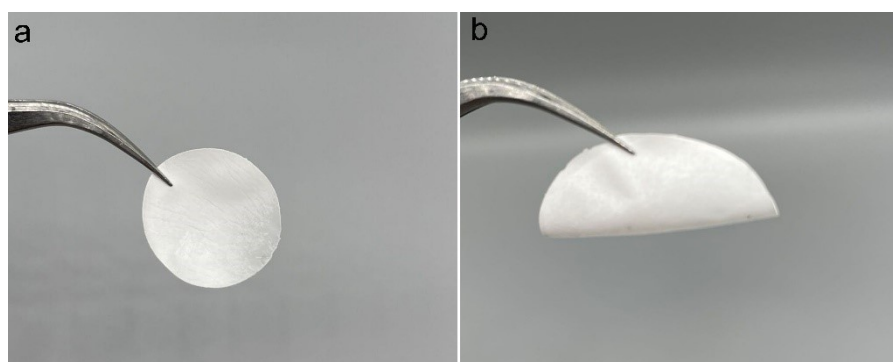


**Fig. S1.** Photographs of a piece of ESM (a) in a flat state and (b) bending state.

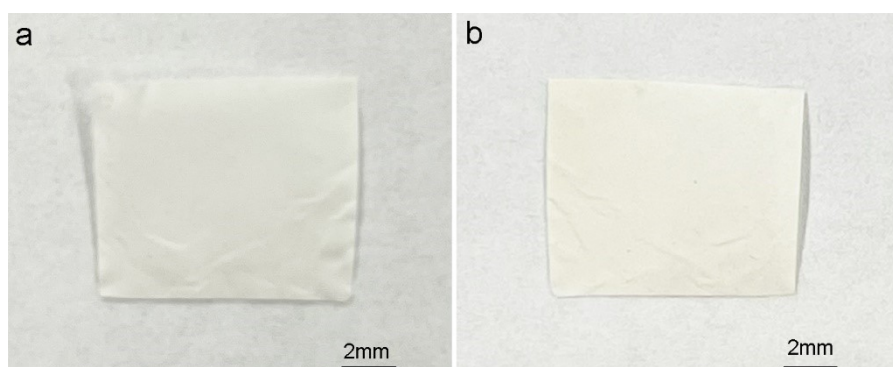


**Fig. S2.** Photographs a piece of (a) ESM and (b) after being heated in an oven at 250 °C for 0.5h. ESM almost remains the same, indicating its good thermal stability and thereby enabling great safety for applications in extreme conditions.

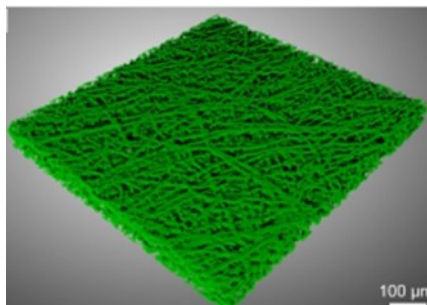


**Fig. S3.** A SR- $\mu$ CT image of fibrous ESM.

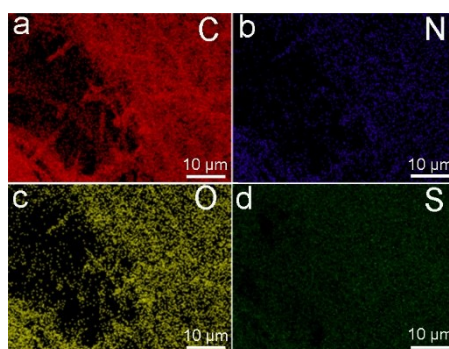


**Fig. S4.** EDS elemental maps of a piece of pristine ESM corresponding to the SEM image in Fig. 1c.

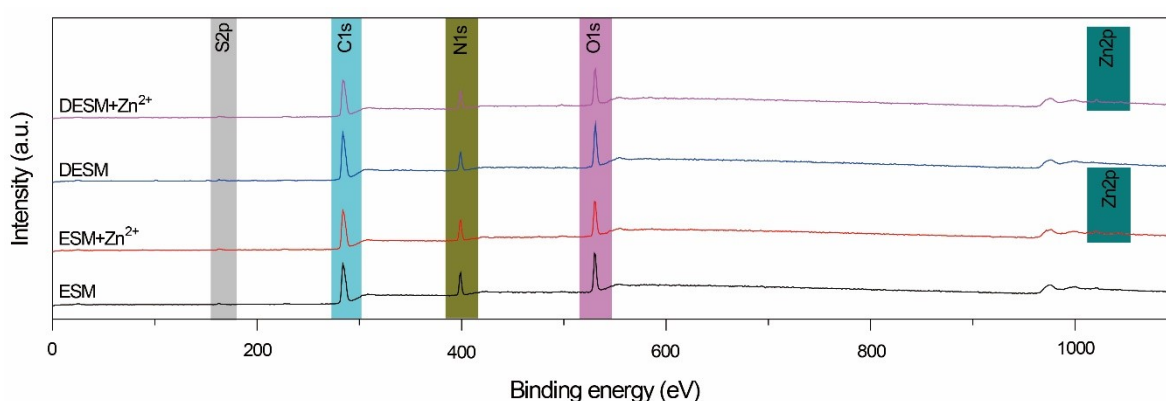


**Fig. S5.** XPS spectra of ESM and DESM before and after absorbing  $Zn^{2+}$ . ESM and DESM were soaked in 2M  $ZnSO_4$  solution for days to fully absorb  $Zn^{2+}$ . Subsequently, they were rinsed with DI water and dried in the air before characterization.

**Table S1.** Chemical contents in ESM and DESM.

	<b>C</b>	<b>N</b>	<b>O</b>	<b>S</b>
<b>ESM</b>	62.83%	15.34%	20.97%	0.86%
<b>DESM</b>	62.46%	15.75%	20.92%	0.87%

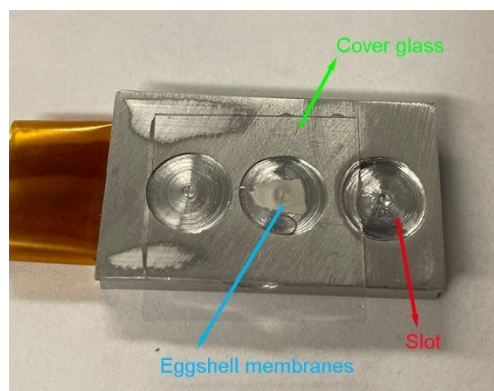


**Fig. S6.** A miniaturized heating set-up allows the in-situ observation of morphology change of ESM during thermal treatment in DI water.

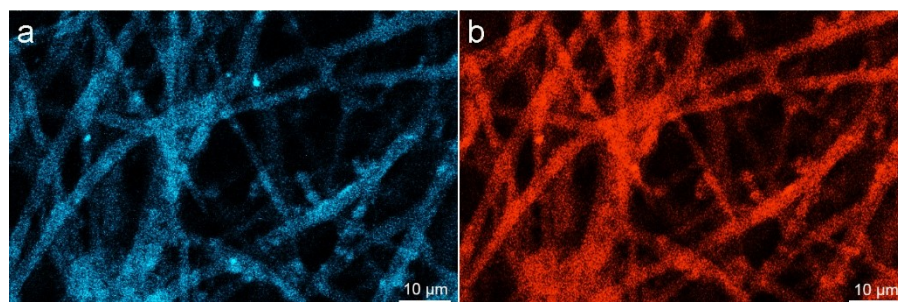


**Fig. S7.** In-situ fluorescence microscopy images of ESM (a) before and (b) after boiling.

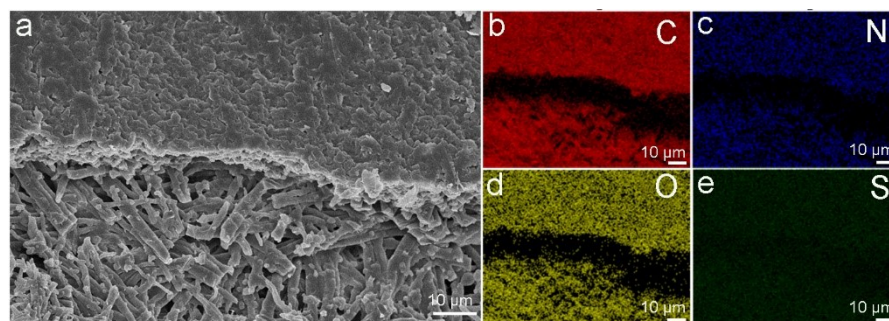


**Fig. S8.** (a) SEM image (c) EDS elemental maps of DESM.

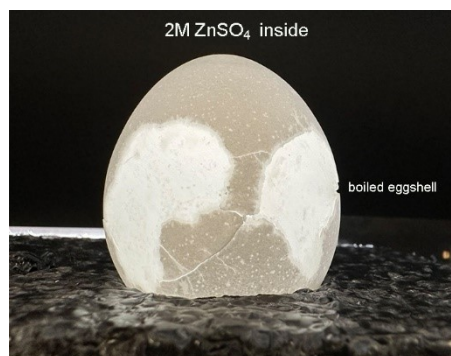


**Fig. S9.** Photograph of a boiled and partially etched eggshell. After boiling, the eggshell in Fig. 1a (right) is still able to hold 2M ZnSO<sub>4</sub> solution.

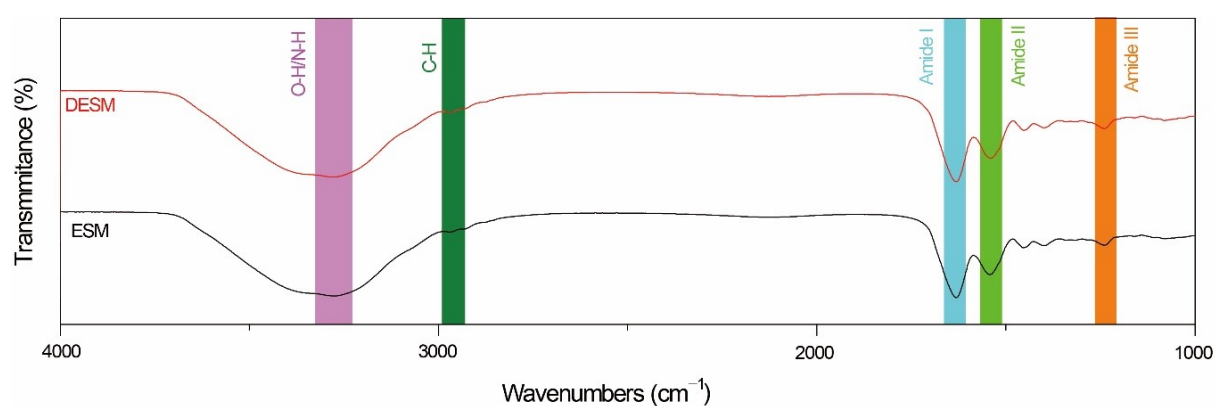


**Fig. S10.** FTIR spectra of ESM and DESM. The band locates at  $\sim 3277\text{ cm}^{-1}$  corresponds to the O-H and N-H stretching vibration, the band at  $\sim 2930\text{ cm}^{-1}$  should be assigned to C-H stretching. The bands at  $\sim 1630$ ,  $\sim 1539$ , and  $\sim 1238\text{ cm}^{-1}$  correspond to the amide I, II, and III. Amide I is mainly due to the C=O stretching vibration ( $\sim 80\%$ ) of the amide groups coupled with little in-plane N-H bending vibration ( $< 20\%$ ).<sup>7</sup> Amide II mainly origin from N-H bending vibration ( $\sim 60\%$ ) together with C-N stretching vibration ( $\sim 30\%$ ) and C-C stretching vibration ( $\sim 10\%$ ). Amide III results from a complex band by several coordinate displacements.<sup>8</sup>

**Table S2.** The proportion of various secondary structures of proteins in ESM and DESM.

	$\beta$ -sheet	Random coil	$\alpha$ -helix	$\beta$ -turn
<b>ESM</b>	53.0%	16.6%	13.0%	17.4%
<b>DESM</b>	56.5%	0.0%	20.1%	23.4%

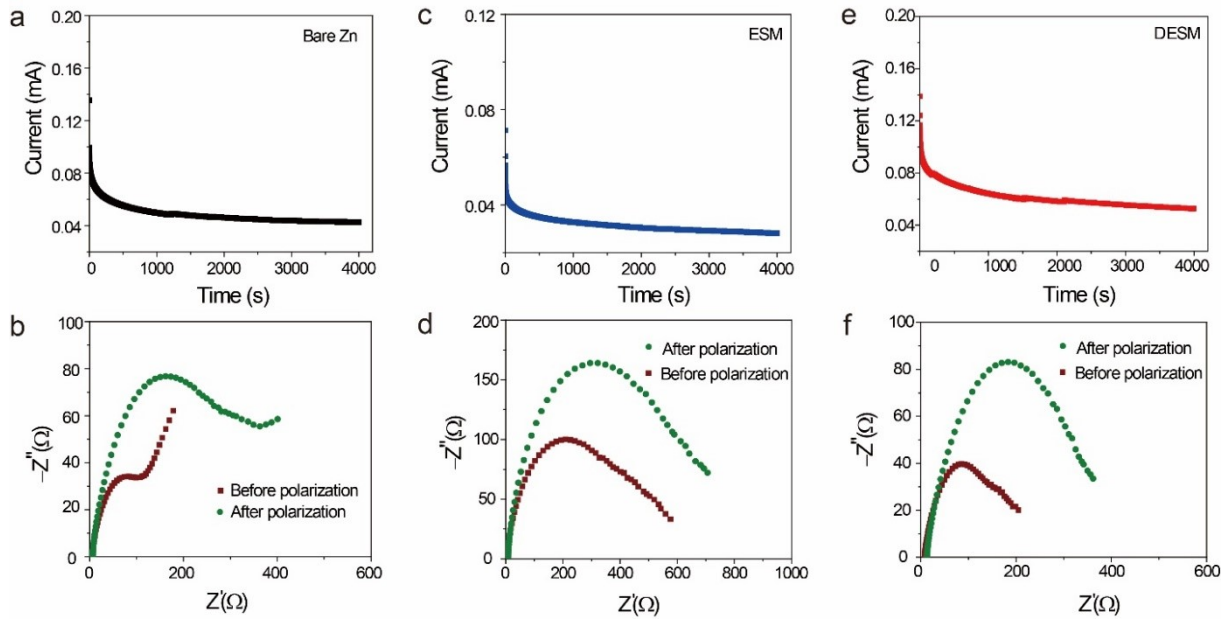


**Fig. S11.** Current-time plots of bare (a) Zn/Zn, (c) Zn@ESM/Zn@ESM, and (e) Zn@DESM/Zn@DESM symmetric cells at a constant potential of 25 mV for 4000 s. The figures below correspond to the Nyquist plots before and after polarization.

**The transference number of  $Zn^{2+}$  was determined by the following equation:<sup>9</sup>**

$$t_{Zn^{2+}} = \frac{I_s(\Delta V - I_0 R_0)}{I_0(\Delta V - I_s R_s)}$$

where  $\Delta V$  is the applied voltage, i.e., 25 mV;  $I_0$  and  $R_0$  are the initial current and resistance, respectively; and  $I_s$  and  $R_s$  are the steady-state current and resistance, respectively. The transference number of  $Zn^{2+}$  in bare Zn/Zn, Zn@ESM/Zn@ESM, and Zn@DESM/Zn@DESM symmetric cells was calculated to be 0.459, 0.533, and 0.645, respectively. A large transference number can reduce the concentration polarization of electrolytes during charge-discharge steps, and thus produce higher power density.<sup>10</sup>

**The concentration of  $Zn^{2+}$  adjacent to DESM:** The density of DESM was measured to be  $0.69 \text{ g cm}^{-3}$ , while the average protein density is  $1.35 \text{ g cm}^{-3}$ .<sup>11</sup> It could be concluded that 48.9 vol% of DESM is void. According to the ICP results in Fig. 1g, 0.77g DESM can adsorb 0.23 g  $Zn^{2+}$ . Therefore, the concentration of  $Zn^{2+}$  adjacent DESM was calculated as follows:

$$\frac{\frac{0.23}{65} \text{ mol}}{\frac{0.77}{0.69} \times 10^{-3} \text{ L}} \times \frac{100\%}{100\% - 48.9\%} = 6.3 \text{ mol/L}$$

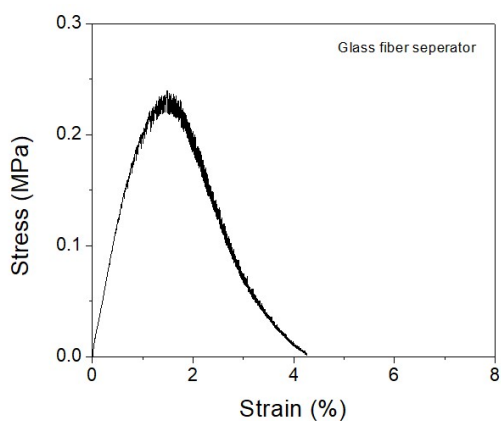


**Fig. S12.** Tensile strength of the glassy fiber separator. The fracture stress and strain of the glass fiber separator are both much inferior to that of both ESM and DESM.

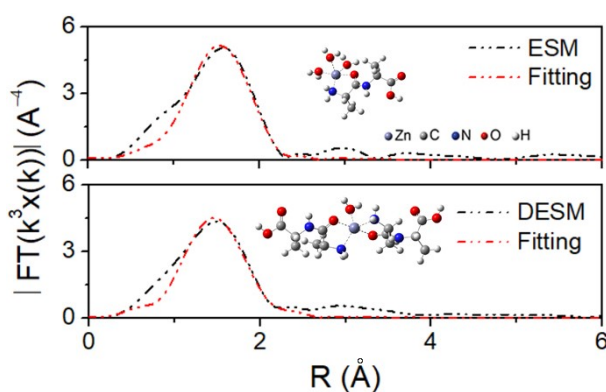


**Fig. S13.** FT-EXAFS fitting curves at R space based on the inserted DFT optimized molecular geometries of  $[\text{Zn}(\text{ALA-ALA})(\text{H}_2\text{O})_3]^{2+}$  (up) and  $[\text{Zn}(\text{ALA-ALA})_2(\text{H}_2\text{O})]^{2+}$  (down). ALA-ALA serves as an exquisite model of the primary structure of eggshell proteins.

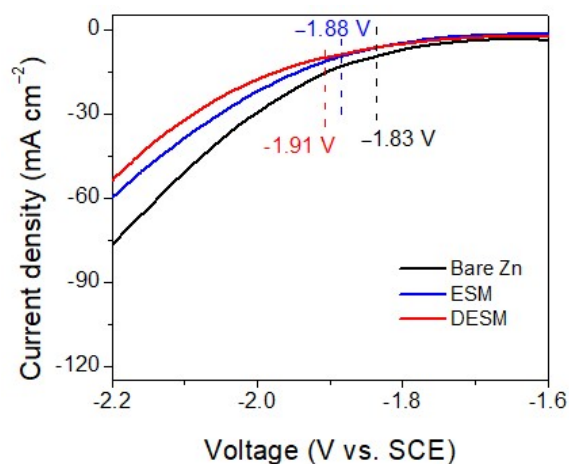


**Fig. S14.** Linear sweep voltammetry curves in 2M  $\text{ZnSO}_4$  as electrolyte. A Pt metal sheet ( $1 \times 1 \text{ cm}^2$ ) with and without ESM/DESM as protection layers was used as the working electrode, a saturated calomel electrode served as the reference electrode, and a graphite rod was used as

the counter electrode. The onsite potential of Bare Zn, ESM- and DESM-protected Zn electrodes are -1.83, -1.88, and -1.91 V, respectively.

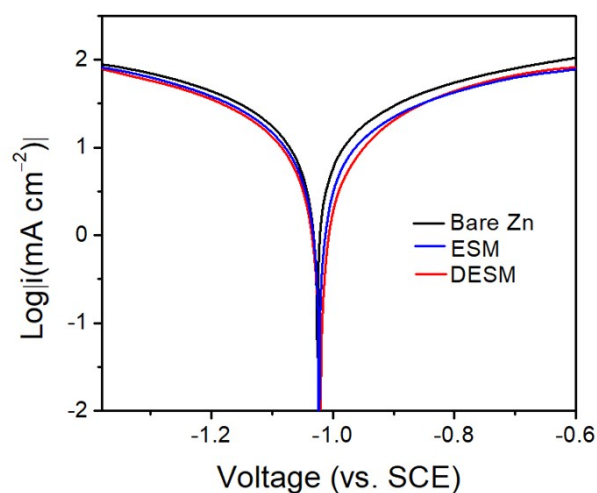


**Fig. S15.** Linear polarization curves showing the corrosion behaviors in the 2M  $\text{ZnSO}_4$  electrolytes with and without ESM/DESM protection.

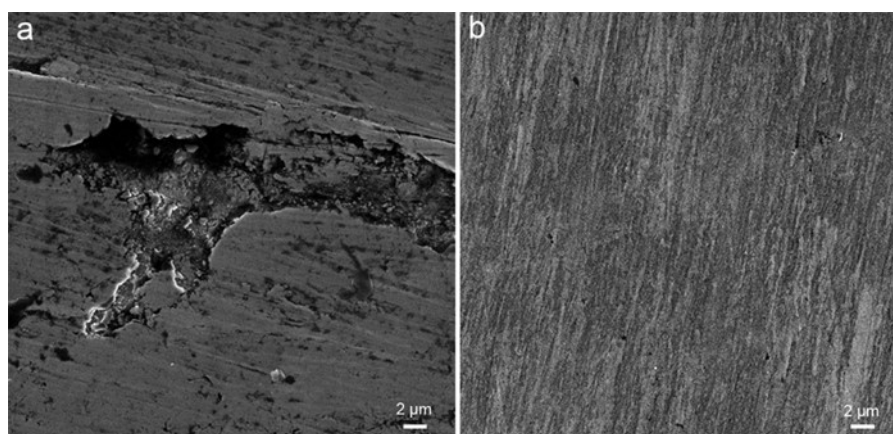


**Fig. S16.** SEM images of unpolished Zn and polished Zn. Once exposed to air, a dense zinc hydroxycarbonate (i.e.,  $\text{Zn}_5(\text{CO}_3)_2(\text{OH})_6$  or  $\text{Zn}_4\text{CO}_3(\text{OH})_6 \cdot \text{H}_2\text{O}$ ) passivation layers forms on the surface of Zn electrodes. These layers have been previously demonstrated to fail in protecting Zn electrodes in aqueous electrolytes, worse yet, increase the energy barrier for Zn stripping/plating.<sup>9</sup> Polishment could remove passivation layers and smooth the surface concurrently, resulting in lower energy barriers for Zn stripping/plating.

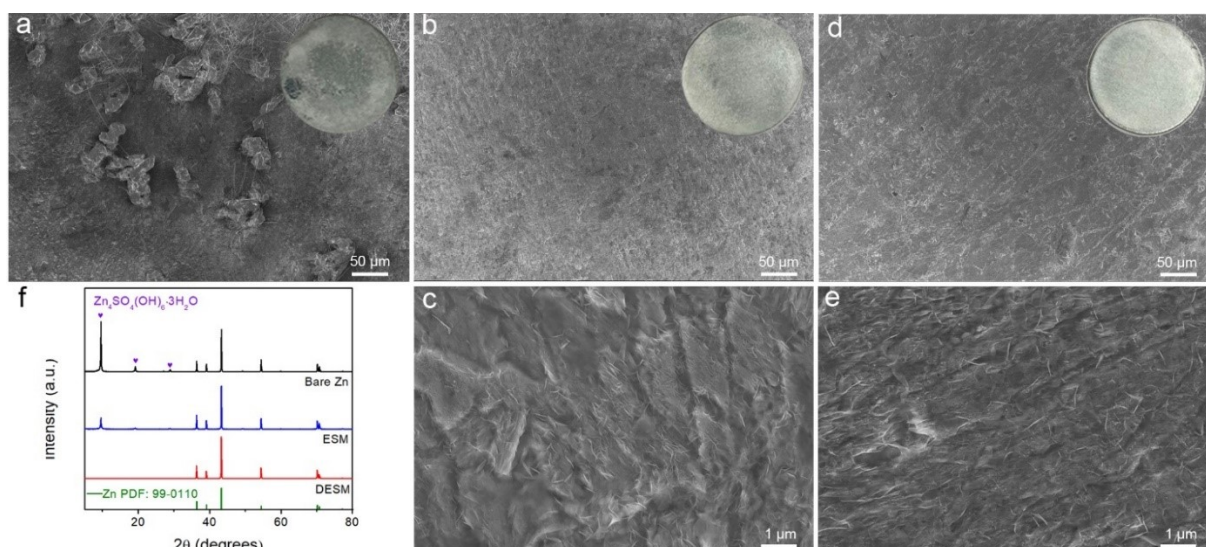


**Fig. S17.** Characterization of the morphology and structure of polished Zn after soaking into 2M ZnSO<sub>4</sub> electrolyte for 2 weeks. The surface SEM images of (a) bare Zn, (b) Zn@ESM, and (c) Zn@DESM. The insets show the corresponding photographs of Zn electrodes. SEM images in c and d are the enlarged view of b and d, respectively. (f) XRD patterns of bare Zn, Zn@ESM, and Zn@DESM.

After soaking into the 2M ZnSO<sub>4</sub> electrolyte for 2 weeks, the bare electrode shows severe color variation and big chunks on the surface. The dark grey regions are believed to be the by-product of side reactions, which are later identified as Zn<sub>4</sub>SO<sub>4</sub>(OH)<sub>6</sub>·3H<sub>2</sub>O by XRD patterns. In contrast, ESM-protected Zn electrodes exhibit a smooth surface and highly inhibited by-products from corrosion reactions after being soaked in aqueous electrolytes, while DESM-protected Zn electrodes remain an even surface almost without Zn<sub>4</sub>SO<sub>4</sub>(OH)<sub>6</sub>·3H<sub>2</sub>O detected, demonstrating the crucial role of DESM in anti-corrosion.

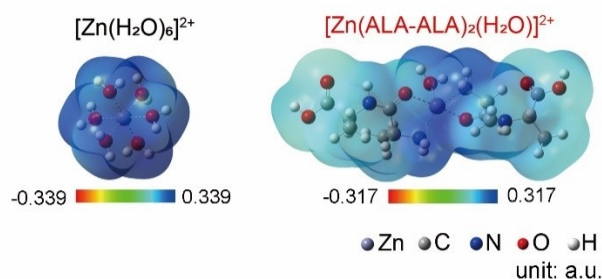


**Fig. S18.** Electrostatic potential of  $[\text{Zn}(\text{H}_2\text{O})_6]^{2+}$  and  $[\text{Zn}(\text{ALA-ALA})_2(\text{H}_2\text{O})]^{2+}$  complexes.

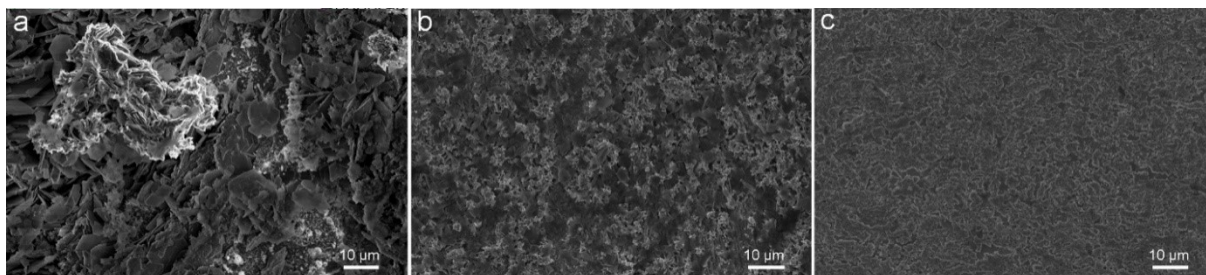


**Fig. S19.** SEM images of Zn electrodes after 10 plating/stripping cycles with a current density of  $2 \text{ mA cm}^{-2}$  with a limited capacity of  $1 \text{ mAh cm}^{-2}$ . (a) bare Zn, (b) Zn@ESM, and (c) Zn@DESM.

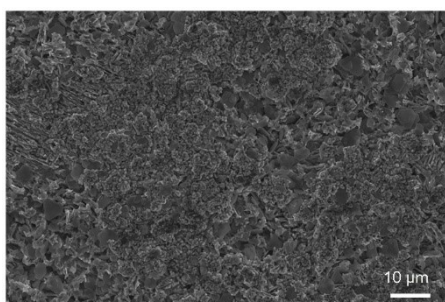


**Fig. S20.** Surface SEM images of Zn@ESM electrodes after cycling at a current density of  $2 \text{ mA cm}^{-2}$  with a limited capacity of  $1 \text{ mAh cm}^{-2}$  after 75 cycles.

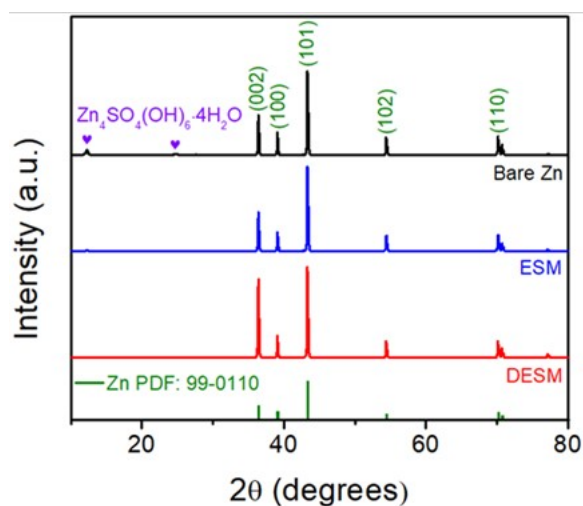


**Fig. S21.** XRD patterns of Zn electrodes after cycling at a current density of  $2 \text{ mA cm}^{-2}$  with a limited capacity of  $1 \text{ mAh cm}^{-2}$  after 75 cycles.

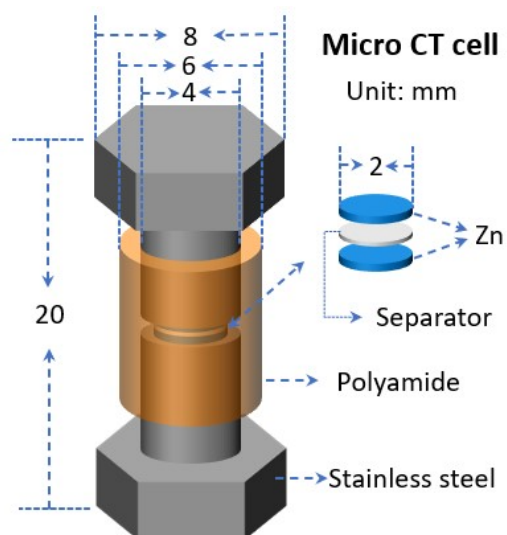


**Fig. S22.** Schematical illustration of the in-situ SR- $\mu$ CT cell.

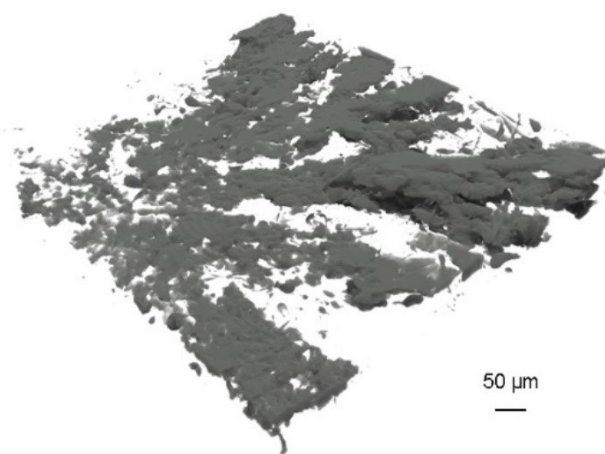


**Fig. S23.** SR- $\mu$ CT images of the Zn-based phase in the glassy fiber separators after long-term cycling in Zn/Zn symmetric cells.

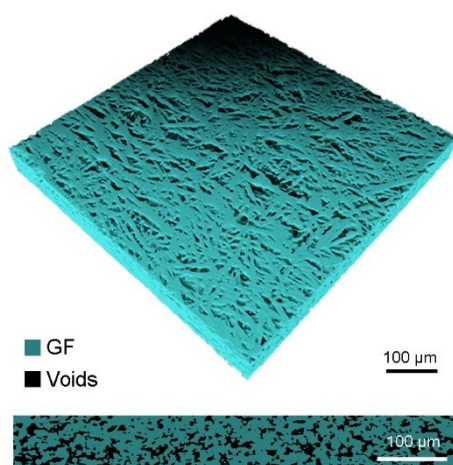


**Fig. S24.** SR- $\mu$ CT images of glass fiber separator after cycling in Zn@DESM/Zn@DESM cells.

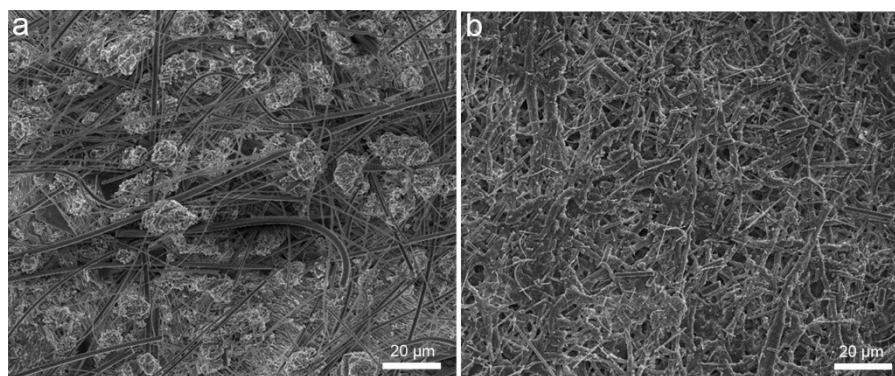


**Fig. S25.** SEM images of (a) glass fiber separator in Zn/Zn symmetric cells and (b) DESM in Zn@DESM/Zn@DESM symmetric cells after long-term cycling.

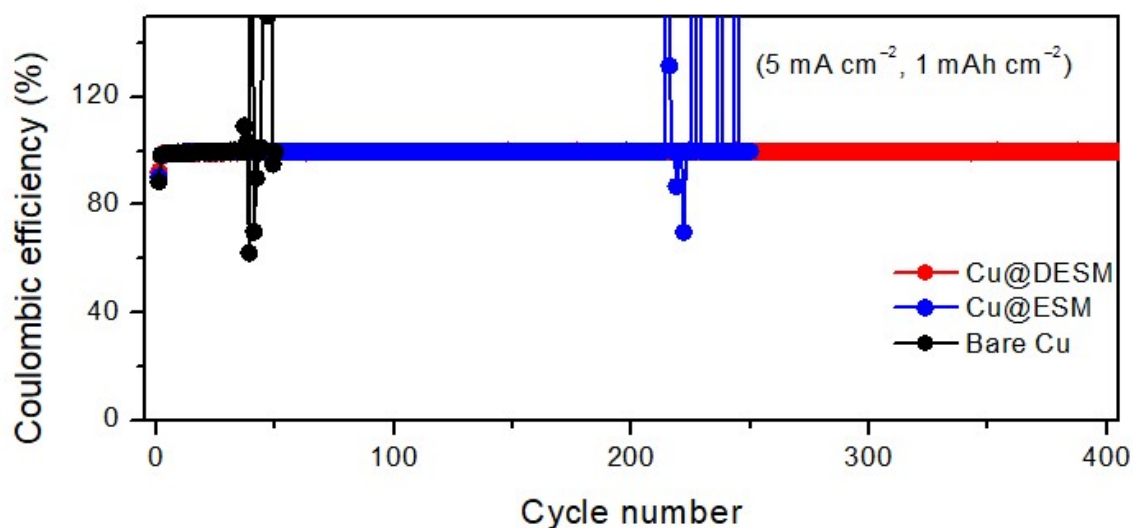


**Fig. S26.** Coulombic efficiency of Zn plating/stripping on bare Cu foil and Cu@ESM, Cu@DESM at a current density of  $5 \text{ mA cm}^{-2}$  with a limited capacity of  $1 \text{ mAh cm}^{-2}$ .

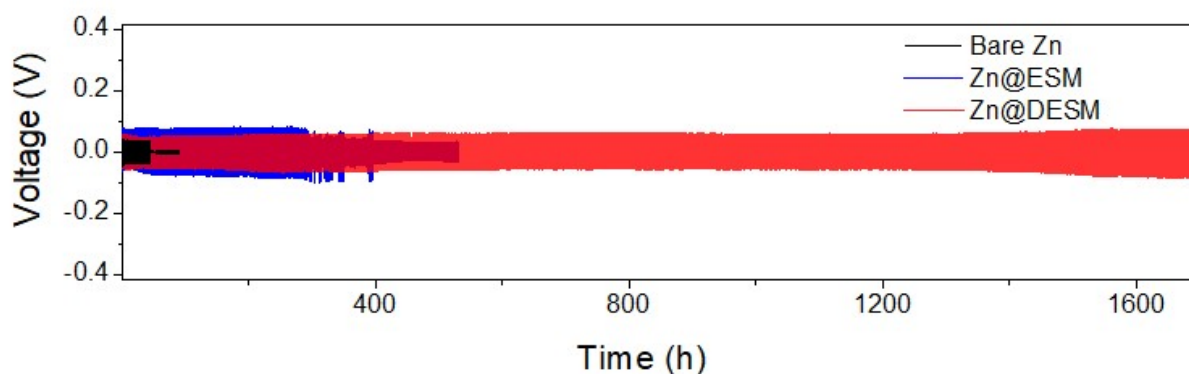


**Fig. S27.** Long-term galvanostatic Zn plating/stripping curves at  $2 \text{ mA cm}^{-2}$  with a limited capacity of  $1 \text{ mAh cm}^{-2}$ .

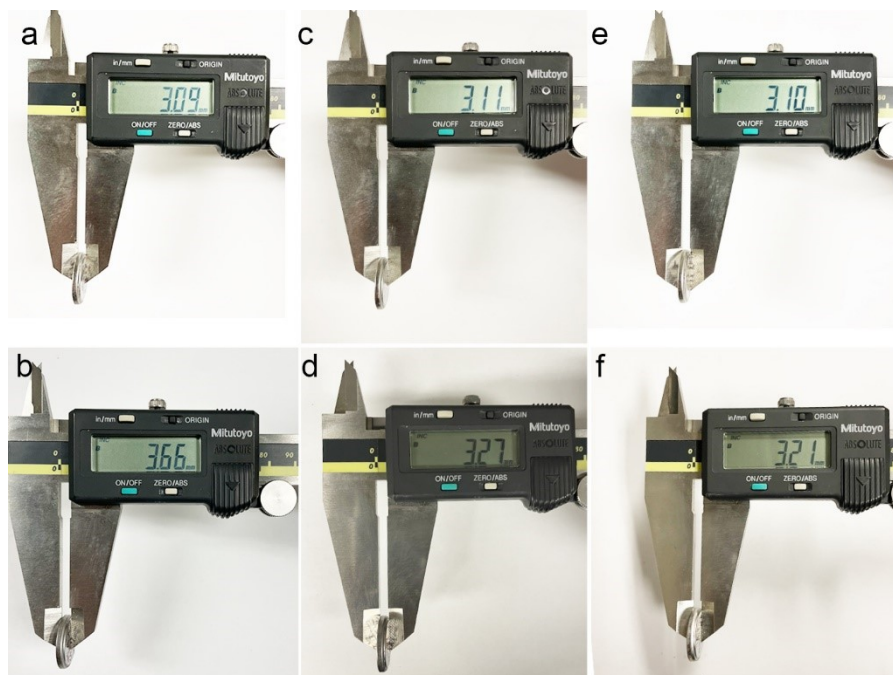


**Fig. S28.** The thickness variation of symmetric Zn cells before (up) and after (down) long-term cycling. The figures from left to right represent bare Zn/Zn, Zn@ESM/Zn@ESM, and Zn@DESM/Zn@DESM symmetric cells, respectively.

The thickness of Zn/Zn cells increases by 18.4%, followed by 5.1% for Zn@ESM/Zn@ESM cells and 3.5% for Zn@DESM/Zn@DESM cells. The thickness increase is a result of the generated  $H_2$  from HER, one main side reaction occurring on Zn anodes in aqueous electrolytes.

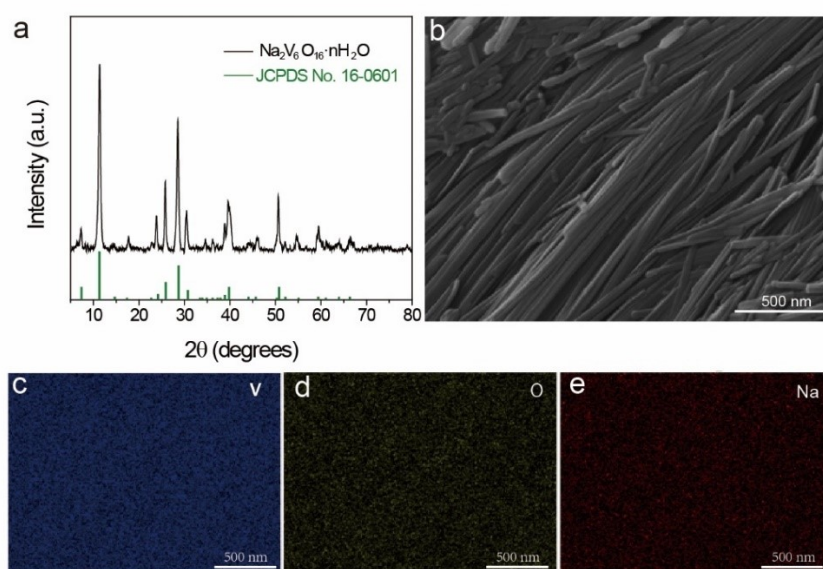


**Fig. S29.** Structural and morphology characterization of as-synthesized NVO. (a) XRD pattern, (b) SEM images, and corresponding EDS elemental maps of V, O, and Na in the synthesized NVO.

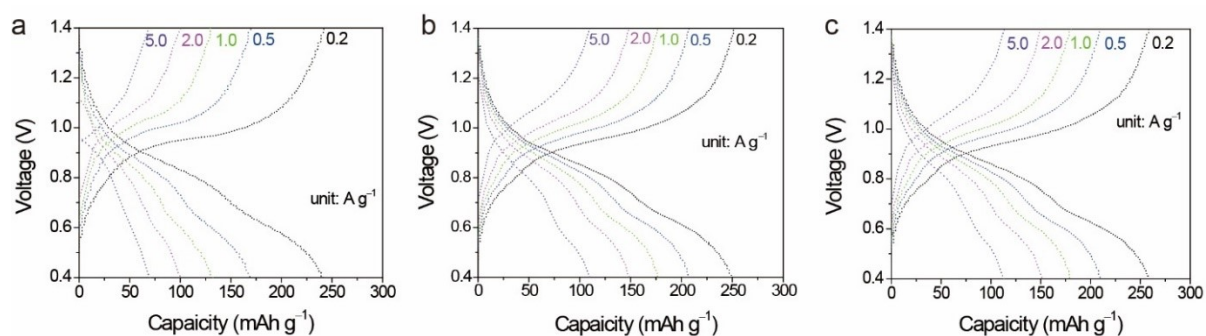


**Fig. S30.** GCD curves of (a) Zn/NVO, (b) Zn@DESM/NVO, and (c) Zn@DESM/NVO@DESM full cells at different current densities. At a considerably high current density of 5 A g<sup>-1</sup>, Zn/NVO, Zn Zn@ESM/NVO, and Zn@DESM/NVO@DESM full cells show a voltage drop of 0.44V, 0.17V, and 0.11V, respectively.

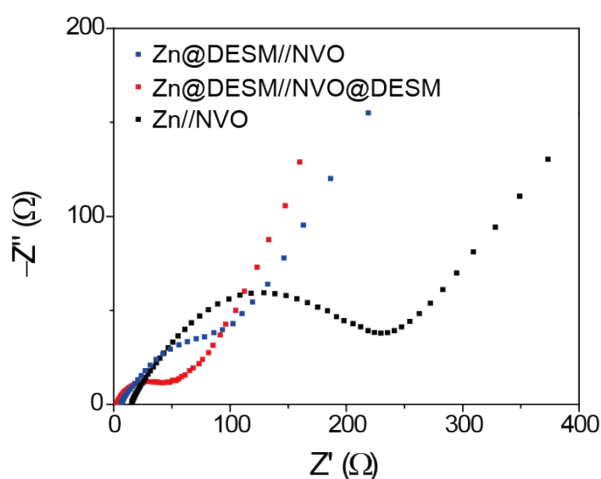


**Fig. S31.** The Nyquist plots of the full cell after long-term cycling.

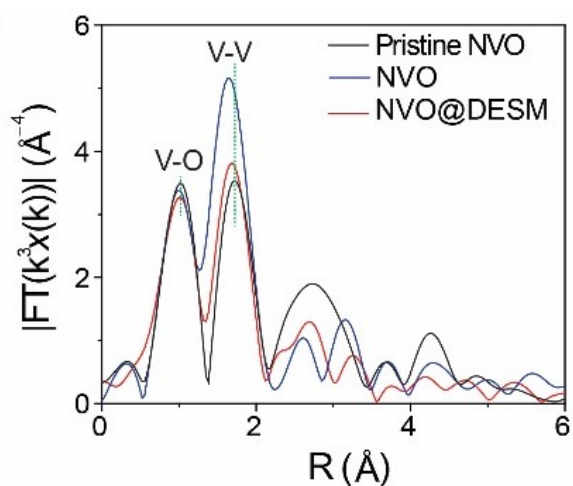


**Fig. S32.** FT  $k^3$ -weighted  $\chi(k)$ -function of the EXAFS spectra for V K-edge in pristine NVO and NVO after long-term cycling in Zn@DESM/NVO, and Zn@DESM/NVO@DESM cells.

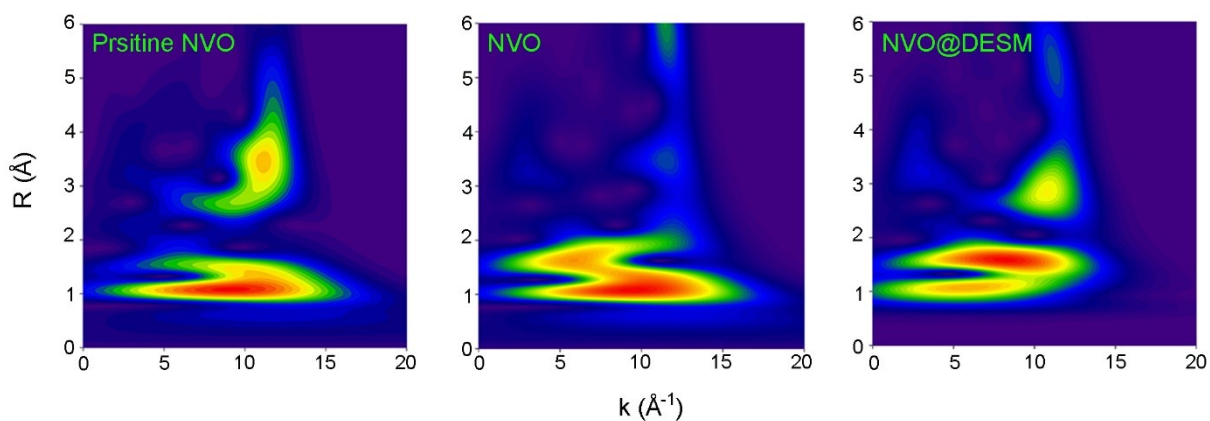


**Fig. S33.** Wavelet transforms for the  $k^3$ -weighted EXAFS signals of pristine NVO (left), and NVO after long-term cycling in Zn@DESM/NVO (middle), and Zn@DESM/NVO@DESM cells (right).

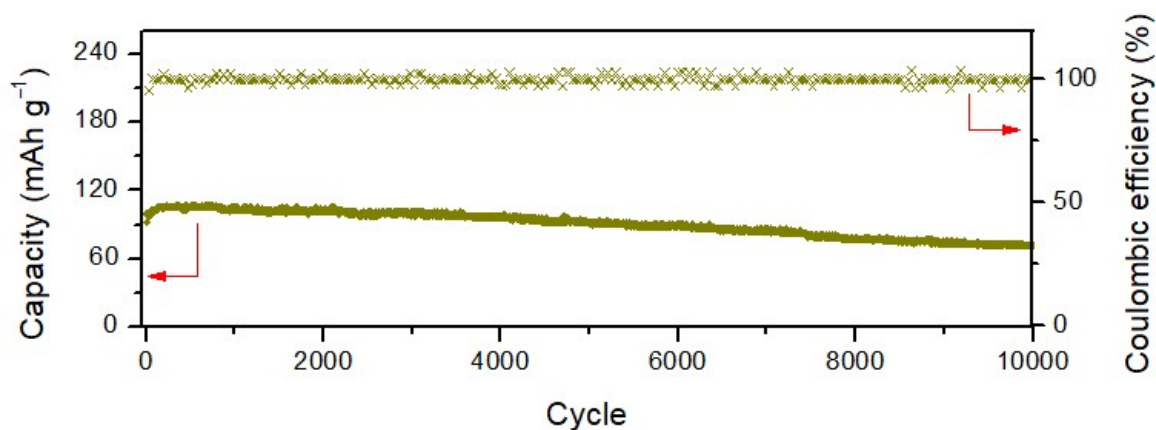


**Fig. S34.** Capacities and CE at different current densities. As-prepared large pieces of DESM paper were used as protective layers in the Zn-NVO full cells.

**Table S3.** Performance comparison of recently reported strategies for stabilizing Zn anodes.

No.	Anode protection strategies	Half cell		Full cell			Ref.	Year
		Cycle lifetime (h@ (mA/cm <sup>2</sup> , mAh/cm <sup>2</sup> ))	Cumulative plated capacity (Ah/cm <sup>2</sup> )	Cell type	Cycle number	Capacity retention (%)		
1	<b>Zn@DESM</b>	<b>5000h@ (0.2, 0.2)</b> <b>1700h @ (2, 1)</b>	<b>0.85</b>	<b>Zn// Na<sub>2</sub>V<sub>6</sub>O<sub>16</sub>·nH<sub>2</sub>O</b>	<b>10000@ 5A/g</b>	<b>100% (2000 cycles)</b> <b>90.1% (10000 cycles)</b>	<b>This work</b>	
2	L-cysteine@Zn	2500h@ (1, 0.5)	0.63	Zn//NH <sub>4</sub> V <sub>4</sub> O <sub>10</sub>	1000@ 5A/g	~70	12	2023
3	Zn@PSPMA	1150h@ (1, 0.5)	0.29	Zn//MnO <sub>2</sub>	800@ 6C	~71.5	13	2023
4	Zn@Co(TAPC)	500@ (20, 1)	0.25	Zn//MnO <sub>2</sub>	5000@2 A/g	NA	14	2023
5	Zn@PDA	1100@ (1, 1)	0.55	Zn//V <sub>2</sub> O <sub>5</sub>	1000@ 1A/g	94.3	15	2021
6	Zn(BF <sub>4</sub> ) <sub>2</sub> + ethylene glycol	4000h@ (0.5, 0.25)	0.50	Zn//V <sub>2</sub> O <sub>5</sub>	800@ 1A/g	60	16	2022
7	DOTf + ZnSO <sub>4</sub>	350@ (4, 4)	0.70	Zn//Zn <sub>0.25</sub> V <sub>2</sub> O <sub>5</sub> ·nH <sub>2</sub> O	1000@ 1.5A/g	83	17	2022
8	PVDF-Sn@Zn	1200h@ (1, 1)	0.60	Zn//MnO <sub>2</sub>	700@ 2A/g	70.3	18	2023
9	ZnSO <sub>4</sub> -C <sub>3</sub> N <sub>4</sub> QDs	1200h@ (1, 1)	0.60	Zn//VOPO <sub>4</sub>	3000@ 1A/g	80.6	19	2022
10	Sn@NHCF	370h@ (1, 1)	0.19	Zn//V <sub>2</sub> O <sub>5</sub>	2200@ 1A/g	NA	20	2022
11	Zn(OTf) <sub>2</sub> + PC	1600 @ (1, 1)	0.80	Zn//ZnMn <sub>2</sub> O <sub>4</sub>	300@ 0.35A/g	80	21	2022
12	Zn@Zn <sub>3</sub> (PO <sub>4</sub> ) <sub>2</sub> and ZnP <sub>2</sub> O <sub>6</sub>	4750@ 1 mA/cm <sup>2</sup>	NA	Zn//V <sub>2</sub> O <sub>5</sub>	4000@5 A/g	82.2	22	2023
13	Pyridine-ZnSO <sub>4</sub> electrolyte	3200@ (2, 2)	3.20	Zn//I <sub>2</sub>	10000@2 A/g	92	23	2023
14	Zn@MXene	800@ (0.2, 0.2)	0.08	Zn//MnO <sub>2</sub>	500@ 1A/g	81	24	2021
15	Pb-Ad@Zn	400h@ (4, 0.5)	0.10	Zn//MnO <sub>2</sub>	400	97	25	2023
16	Zn@3D Cu branches@ CaTiO <sub>3</sub>	800h@ (1, 1)	0.40	Zn//V <sub>10</sub> O <sub>24</sub> ·12H <sub>2</sub> O	500@ 2A/g	48.2	26	2022
17	Zn@COF	400@ (1, 1)	0.20	Zn//MnO <sub>2</sub>	300@ 2A/g	88.5	27	2021
18	Zn@ZnF <sub>2</sub>	500@ (0.5, 1)	0.25	Zn//MnO <sub>2</sub>	2000@ 10A/g	96	28	2021
19	Zn@Sn	500@ (1, 1)	0.25	NA	NA	NA	29	2021
20	Zn@GO	1200@ (1, 1)	0.60	Zn//LiMn <sub>2</sub> O <sub>4</sub>	178@ 1C	80	30	2021
21	Zn@PFSA	1500@ (1, 0.5)	0.38	Zn//MnO <sub>2</sub>	300@ 2C	NA	31	2022
22	Zn@ (Ca <sub>5</sub> (PO <sub>4</sub> ) <sub>3</sub> (OH))	2400@ (0.1, 0.1)	0.12	Zn//MnO <sub>2</sub>	1600@ 1 A/g	95.3	32	2022
23	Cu(100)@Zn	550@ (1, 1)	0.28	Zn//MnO <sub>2</sub>	548@ 0.2 A/g	88.7	33	2022
24	Tripropylene glycol + ZnSO <sub>4</sub> electrolyte	1100 (1, 0.5)	0.28	Zn//MnO <sub>2</sub>	1000@ 2 A/g	NA	34	2023

## References

1. D. C. Koningsberger and R. Prins, 1987.
2. B. Ravel and M. Newville, *J. Synchrotron Radiat.*, 2005, **12**, 537-541.
3. M. Frisch, G. Trucks, H. Schlegel, G. Scuseria, M. Robb, J. Cheeseman, G. Scalmani, V. Barone, G. Petersson and H. Nakatsuji, 2009.
4. C. Lee, W. Yang and R. G. Parr, *Phys. Rev. B*, 1988, **37**, 785.
5. Y. Zhao and D. G. Truhlar, *Theor. Chem. Acc.*, 2008, **120**, 215-241.
6. J. Tomasi and M. Persico, *Chem. Rev.*, 1994, **94**, 2027-2094.
7. S. Krimm and J. Bandekar, *Adv. Protein Chem.*, 1986, **38**, 181-364.
8. G. Long, Y. Ji, H. Pan, Z. Sun, Y. Li and G. Qin, *Int. J. Food Prop.*, 2015, **18**, 763-774.
9. J. Hao, B. Li, X. Li, X. Zeng, S. Zhang, F. Yang, S. Liu, D. Li, C. Wu and Z. Guo, *Adv. Mater.*, 2020, **32**, 2003021.
10. L. Ye and Z. Feng, in *Polymer Electrolytes*, Elsevier, 2010, pp. 550-582.
11. H. Fischer, I. Polikarpov and A. F. Craievich, *Protein Sci.*, 2004, **13**, 2825-2828.
12. D. Li, Y. Tang, S. Liang, B. Lu, G. Chen, J. J. E. Zhou and E. Science, *Energy Environ. Sci.*, 2023, **16**, 3381-3390.
13. H. Liu, Q. Ye, D. Lei, Z. Hou, W. Hua, Y. Huyan, N. Li, C. Wei, F. Kang, J.-G. J. E. Wang and E. Science, *Energy Environ. Sci.*, 2023, **16**, 1610-1619.
14. K. Zhu, C. Guo, W. Gong, Q. Xiao, Y. Yao, K. Davey, Q. Wang, J. Mao, P. Xue, Z. J. E. Guo and E. Science, *Energy Environ. Sci.*, 2023, **16**, 3612-3622.
15. X. Zeng, K. Xie, S. Liu, S. Zhang, J. Hao, J. Liu, W. K. Pang, J. Liu, P. Rao, Q. J. E. Wang and E. Science, *Energy Environ. Sci.*, 2021, **14**, 5947-5957.
16. D. Han, C. Cui, K. Zhang, Z. Wang, J. Gao, Y. Guo, Z. Zhang, S. Wu, L. Yin and Z. J. N. S. Weng, *Nat. Sustain.*, 2022, **5**, 205-213.
17. C. Li, A. Shyamsunder, A. G. Hoane, D. M. Long, C. Y. Kwok, P. G. Kotula, K. R. Zavadil, A. A. Gewirth and L. F. J. J. Nazar, *Joule*, 2022, **6**, 1103-1120.
18. Q. Cao, Y. Gao, J. Pu, X. Zhao, Y. Wang, J. Chen and C. J. N. C. Guan, *Nat. Commun.*, 2023, **14**, 641.
19. W. Zhang, M. Dong, K. Jiang, D. Yang, X. Tan, S. Zhai, R. Feng, N. Chen, G. King and H. Zhang, *Nat. Commun.*, 2022, **13**, 1-12.
20. H. Yu, Y. Zeng, N. W. Li, D. Luan, L. Yu and X. W. J. S. A. Lou, *Sci. Adv.*, 2022, **8**, eabm5766.
21. F. Ming, Y. Zhu, G. Huang, A.-H. Emwas, H. Liang, Y. Cui and H. N. J. J. o. t. A. C. S. Alshareef, *J. Am. Chem. Soc.*, 2022, **144**, 7160-7170.
22. S. Liu, J. Vongsvivut, Y. Wang, R. Zhang, F. Yang, S. Zhang, K. Davey, J. Mao and Z. J. A. C. Guo, *Angew. Chem. Int. Ed.*, 2023, **135**, e202215600.
23. Y. Lyu, J. A. Yuwono, P. Wang, Y. Wang, F. Yang, S. Liu, S. Zhang, B. Wang, K. Davey and J. J. A. C. I. E. Mao, *Angew. Chem. Int. Ed.*, 2023, **62**, e202303011.
24. N. Zhang, S. Huang, Z. Yuan, J. Zhu, Z. Zhao and Z. Niu, *Angew. Chem. Int. Ed.*, 2021, **133**, 2897-2901.
25. P. Ruan, X. Chen, L. Qin, Y. Tang, B. Lu, Z. Zeng, S. Liang and J. J. A. M. Zhou, *Adv. Mater.*, 2023, **35**, 2300577.
26. Z. Zhang, X. Yang, P. Li, Y. Wang, X. Zhao, J. Safaei, H. Tian, D. Zhou, B. Li and F. J. A. M. Kang, *Adv. Mater.*, 2022, **34**, 2206970.
27. J. H. Park, M. J. Kwak, C. Hwang, K. N. Kang, N. Liu, J. H. Jang and B. A. J. A. M. Grzybowski, *Adv. Mater.*, 2021, **33**, 2101726.
28. Y. Yang, C. Liu, Z. Lv, H. Yang, Y. Zhang, M. Ye, L. Chen, J. Zhao and C. C. J. A. M. Li, *Adv. Mater.*, 2021, **33**, 2007388.
29. S. Li, J. Fu, G. Miao, S. Wang, W. Zhao, Z. Wu, Y. Zhang and X. J. A. M. Yang, *Adv. Mater.*, 2021, **33**, 2008424.

30. J. Zhou, M. Xie, F. Wu, Y. Mei, Y. Hao, R. Huang, G. Wei, A. Liu, L. Li and R. J. A. M. Chen, *Adv. Mater.*, 2021, **33**, 2101649.
31. L. Hong, X. Wu, L.-Y. Wang, M. Zhong, P. Zhang, L. Jiang, W. Huang, Y. Wang, K.-X. Wang and J.-S. J. A. n. Chen, *ACS Nano*, 2022, **16**, 6906-6915.
32. K. Qi, W. Zhu, X. Zhang, M. Liu, H. Ao, X. Wu and Y. J. A. n. Zhu, *ACS Nano*, 2022, **16**, 9461-9471.
33. Y. Yan, C. Shu, T. Zeng, X. Wen, S. Liu, D. Deng and Y. J. A. n. Zeng, *ACS Nano*, 2022, **16**, 9150-9162.
34. Z. Liu, R. Wang, Q. Ma, J. Wan, S. Zhang, L. Zhang, H. Li, Q. Luo, J. Wu and T. J. A. F. M. Zhou, *Adv. Funct. Mater.*, 2023, 2214538.